Chinese Journal of Structural Chemistry

ARTICLE

S-scheme Porous g-C_3N_4/Ag_2MoO_4 Heterojunction Composite for CO_2 Photoreduction

Zhongliao Wang[1], Ruilian Liu[1], Jinfeng Zhang[1]* and Kai Dai[1]*

[1]*Key Laboratory of Green and Precise Synthetic Chemistry and Applications, Ministry of Education, Anhui Province Key Laboratory of Pollutant Sensitive Materials and Environmental Remediation, School of Physics and Electronic Information, Huaibei Normal University, Huaibei 235000, China*

ABSTRACT Utilizing solar energy to achieve artificial photosynthesis of chemical fuel is prevalent in tackling excessive CO_2 emission and fossil fuel depletion. Grievous charge recombination and weak redox capability aggravate the CO_2 photoreduction performance. Engineering tailored morphology and constructing matched heterostructure are two significant schemes to ameliorate the CO_2 photoconversion efficiency of g-C_3N_4-based composite. Herein, a novel S-scheme ultrathin porous g-C_3N_4 (UPCN)/Ag_2MoO_4 (AMO) composite was designed by in-situ growing tetragonal α-AMO nanoparticles (NPs) (5-30 nm) on UPCN nanosheets (NSs). The S-scheme charge transfer route endows UPCN/AMO with fast charge separation and strong redox capability, demonstrated by X-ray photoelectron spectroscopy (XPS), photoelectrochemical tests, steady-state and time-resolved photoluminescence (PL) spectra, and DFT calculations. The UPCN/AMO composite exhibits elevated CO_2 photoreduction performance with CO and CH_4 yield rates of 6.98 and 0.38 μmol g^{-1} h^{-1}, which are 3.5 and 2.9 folds higher than that of pristine UPCN, respectively. Finally, the CO_2 photoreduction intermediates are analyzed, and the CO_2 photoreduction mechanism is discussed. This work provides a reference for various g-C_3N_4-based composites applied in artificial photosynthesis.

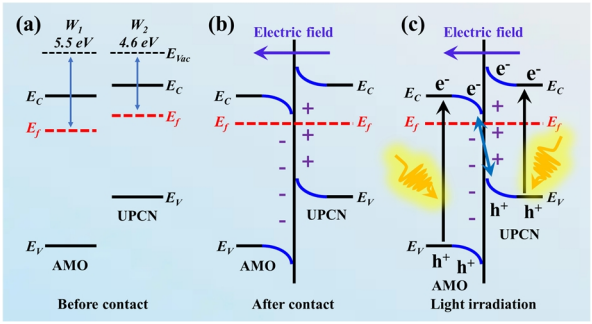

Keywords: S-scheme, g-C_3N_4, Ag_2MoO_4, heterojunction, CO_2 photoreduction

n INTRODUCTION

Photocatalytic CO_2 reduction to carbonaceous fuel is a rewarding project for CO_2 accumulation and fossil resource depletion.[1-3] Nevertheless, the grievous charge recombination and weak redox capability still slack CO_2 photoreduction research pace.[4-7] For one thing, CO_2 photoconversion to hydrocarbon fuels involves an uphill reaction that needs high activation energy.[8-10] For another, CO_2 photoreduction needs the synergistic effect of the photogenerated holes and electrons.[11-13] It requires that the electrons on the conduction band (CB) possess sufficient reductive capability to activate the CO_2 molecules, and the holes on the valance band (VB) possess enough oxidative power to produce protons by oxidizing water.[14-17] In this way, a pristine semiconductor whose energy is appropriate for carbon dioxide reduction has a wide bandgap, which is detrimental for the utilization of visible light.[18-25] S-scheme heterojunction photocatalysts can simultaneously accomplish fast charge separation and strong redox ability, potentially appealing for improved CO_2 photoreduction performance.[1]

Recently, g-C_3N_4 (CN) has served as a CO_2 photoreduction candidate due to an appropriate bandgap of about 2.7 eV and negative CB potential.[26-28] The CO_2 photoreduction activity of pristine CN remains undisireble due to the fast charge recombination and weak oxidative capability.[29,30] Therefore, developing a novel S-scheme CN-based composite remains imperative to ameliorate charge separation and redox ability for improved CO_2 photoreduction performance.[14,31,32] Some CN-based composites, such as g-C_3N_4/ZnO,[17] TiO_2/C_3N_4/Ti_3C_2 Mxene,[33] g-C_3N_4/$Zn_{0.2}Cd_{0.8}S$,[34] g-C_3N_4/Sn_2S_3-DETA,[35] $Cu_2V_2O_7$/g-C_3N_4,[36] Au@Void@g-C_3N_4/SnS,[37] and $LaPO_4$/g-C_3N_4,[38] were fabricated for ameliorating CO_2 photoreduction performance. To further understand the CO_2 photoreduction mechanism and improve the CO_2 photoreduction performance, more novel oxidative photocatalysts are worthwhile to be developed. Ag_2MoO_4 (AMO) exhibits outstanding photodegradation and antibacterial performance owing to a positive VB level.[39,40] Meanwhile, the band structure of AMO theoretically matches well with that of CN.[41] Thereby, it is feasible to design an S-scheme CN/AMO composite to raise the CO_2 photoreduction efficiency.

Inspired by this, the ultrathin porous g-C_3N_4 (UPCN)/AMO was fabricated by annealing and in-situ growing routes. The S-scheme UPCN/AMO heterojunction was discovered by X-ray photoelectron spectroscopy (XPS) and work function calculation. Benefited from S-scheme heterojunction, the internal electric field (IEF) provides a driven force for photoexcited electrons to migrate from AMO CB to UPCN VB. Consequently, the charge with weak redox capability will recombine driven by IEF, and the charge with elevated redox capability will be reserved and involved in the CO_2 photoreduction reaction. Meanwhile, with S-scheme heterojunction and ultrathin sheet-like structure, the oxidation reaction will occur on AMO nanoparticles (NPs), and the reduction reaction will proceed on UPCN nanosheets (NSs), which achieves spatial charge separation. The advanced charge separation efficiency was also verified by photoelectrochemical tests, steady-state and time-resolved photoluminescence (SSPL and TRPL) spectra. As expected, the UPCN/AMO composite elevated CO_2 photoreduc-

© 2022 fjirsm, CAS, Fuzhou

DOI: 10.14102/j.cnki.0254-5861.2022-0108

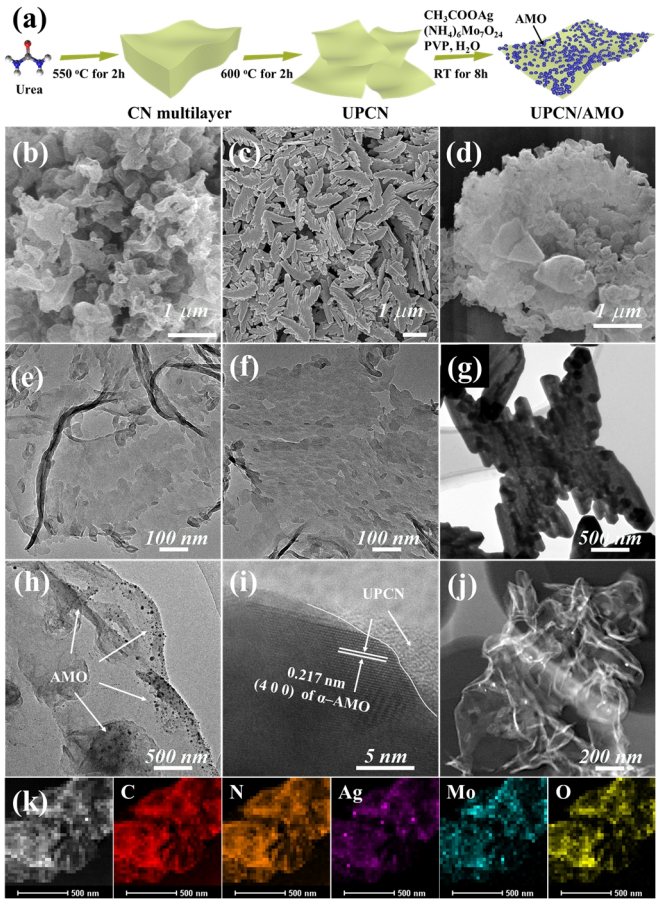

Figure 1. (a) Diagram illustration for the formation process of UPCN/AMO composite; FESEM images of (b) UPCN NSs, (c) AMO NSs and (d) UPCN/AMO composite; TEM images of (e,f) UPCN NSs, (g) AMO NSs and (h) UPCN/AMO composite; (i) HRTEM image, (j,k) HAADF image and corresponding elements mappings of UPCN/AMO composite.

tion performance compared with UPCN. Subsequently, the CO_2 photoreduction intermediates were unveiled by in-situ diffuse reflectance infrared Fourier transform spectroscopy (DRIFTS), which is a vital reference for the CO_2 photoreduction process. Eventually, the CO_2 photoreduction mechanism of the UPCN/AMO composite was proposed.

n RESULTS AND DISCUSSION

The preparation processes of the UPCN/AMO composite are vividly illustrated in Figure 1a. Firstly, multilayered CN was fabricated by controllably calcining pure urea at 550 °C in a muffle furnace. These multilayered CN will dissociate into UPCN during the secondary calcination route at 600 °C. This UPCN surface is negatively charged,[42] which is conducive to the adsorption of Ag^+ ions.[43-47] The adsorbed Ag^+ ions will serve as the nucleation site of AMO so that AMO NPs can intimately grow on UPCN NSs to form UPCN/AMO composite. The UPCN NSs are curly and porous with a thickness of 1.05 nm (Figure 1b,e,f and Figure S1). Instead, the pristine AMO NSs are butterfly-like with a thickness of about dozens of nanometers (Figure 1c,g). The UPCN/AMO composite morphology is not significantly distinct from pristine AMO NSs (Figure 1d). Because when AMO in situ grows on UPCN NSs, it will not grow into nanosheets but into small nanoparticles with a diameter of several to dozens of nanometers (Figure 1h). Moreover, a clear lattice fringe with an interplanar spacing of 0.217 nm can readily correspond to the (400) plane of α-AMO. In addition, an apparent interface between α-AMO and amorphous UPCN marked with a white curve can be observed (Figure 1i). Meanwhile, the bright white spots on curved UPCN NSs can originate from AMO NPs, which further verifies the formation of UPCN/AMO heterojunction (Figure 1j). Five elements of C, N, Ag, Mo, and O are displayed on the scan region of HAADF-STEM (Figure 1k). The elements distribution region matched well with the UPCN/AMO sample, further demonstrating that AMO NPs successfully anchor on the UPCN surface.

The phase of AMO, UPCN, and UPCN/AMO composite was detected by XRD (Figure 2a). The diffraction peaks of pristine AMO can be assigned to tetragonal α-AMO and cubic AMO (JCPDS No. 21-1340 and 08-0473), of which α-AMO is the main phase.[39,48] A weak diffraction peak of UPCN at 2θ = 27.4° caused by interplanar stacking can correspond with the (002) crystal plane of UPCN.[49,50] The broad diffraction peak also indicates the multilayered UPCN was dissociated into UPCN NSs. The diffraction peaks of UPCN/AMO are similar to that of pristine AMO, but the ratio of cubic AMO slightly increases. The diameter of cubic AMO is smaller than that of tetragonal α-AMO, which also illustrates that when AMO grows on UPCN, its size will decrease to form NPs rather than be butterfly-like NSs.[48,51] Regretfully, the diffraction peak of UPCN NSs fails to be observed on the diffraction peaks of the UPCN/AMO composite. Therefore, the FT-IR spectra were employed to evidence the existence of UPCN NSs (Figure 2b). For UPCN NSs, the absorption peak at 808 cm^{-1} originates from the breathing mode of s-triazine rings.[52] The absorption peaks between 1130 and 1720 cm^{-1} correspond to C-N stretching vibration and heptazine-based structure.[53] The absorption peaks in the 2920-3460 cm^{-1} range derive from amidogen

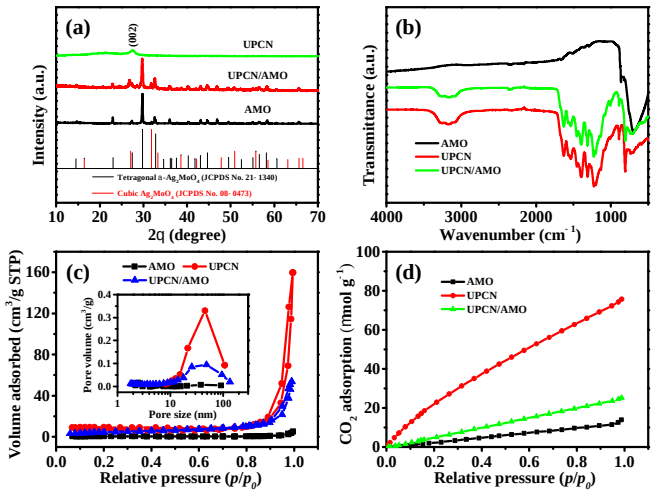

Figure 2. (a) XRD patterns, (b) FT-IR spectra, (c) N_2 adsorption-desorption isotherms and corresponding pore-size distribution (inset), and (d) CO_2 adsorption isotherms of AMO, UPCN and UPCN/AMO composite.

© 2022 fjirsm, CAS, Fuzhou
Chin. J. Struct. Chem. **2022**, 41, 2206015-2206022
DOI: 10.14102/j.cnki.0254-5861.2022-0108

and hydroxyl groups.[54] For AMO, the absorption peak at 681 cm^{-1} results from the stretching vibration of the Mo-O octahedron.[55] The absorption peaks of UPCN/AMO composite exhibit strong signals of UPCN, evidencing the existence of UPCN. In addition, the UPCN of UPCN/AMO composite can also be detected by electron paramagnetic resonance (EPR) spectroscopy (Figure S2). No apparent EPR signal for AMO can be observed, indicating few defects. Instead, a strong EPR signal with a g value of 2.005 for pristine UPCN can be ascribed to aromatic circulation in tri-s-triazine structures of UPCN. The UPCN/AMO composite exhibits a stronger EPR adsorption peak, denoting that AMO can trigger the charge delocalization of UPCN, thus benefiting charge separation.[56] The nitrogen adsorption-desorption isotherms and hysteresis loop of UPCN, AMO, and UPCN/AMO can be classified into type IV and H3, uncovering mesoporous capillary condensation and slit-type pores from curved NSs (Figure 2c).[57-59] The UPCN exhibits a higher specific surface area, larger volume, and stronger CO_2 adsorption due to ultrathin porous sheet-like structure than pristine AMO (Figure 2c,d and Table S1). In contrast, the UPCN/AMO shows a lower specific surface area, pore volume, and weak CO_2 adsorption ability than pristine UPCN, demonstrating the successful load of AMO NPs on UPCN NSs.

The elemental ingredients and chemical states were investigated by XPS. The C 1s and N 1s orbitals match well with pristine UPCN, and the Ag 3d, Mo 3d, and O 1s orbitals are linked to pristine AMO (Figure 3a). The absorption peaks of UPCN/AMO composite can be readily indexed to pristine UPCN and AMO, and no other impurity can be observed, indicating the successful preparation of UPCN/AMO composite. The three characteristic peaks

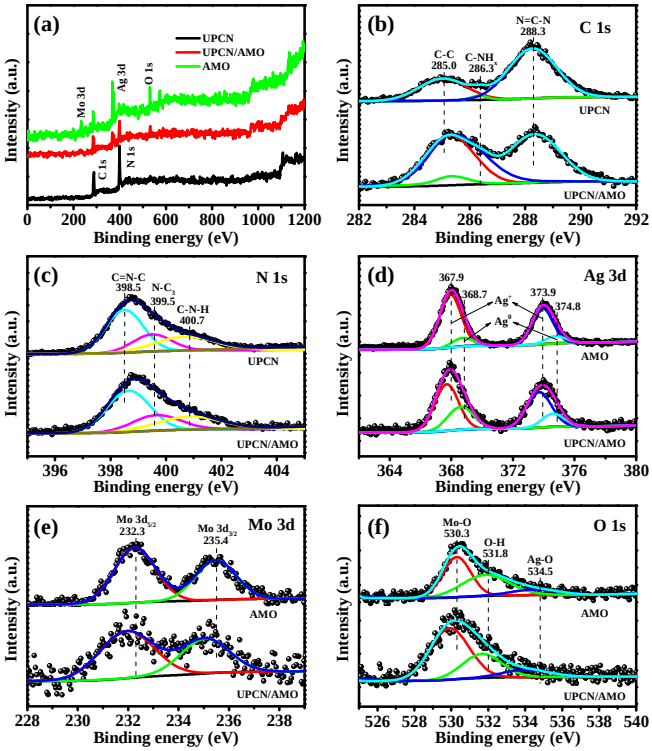

Figure 3. (a) Survey spectra; High-resolution XPS spectra of (b) C 1s, (c) N 1s, (d) Ag 3d, (e) Mo 3d and (f) O 1s orbitals of various samples.

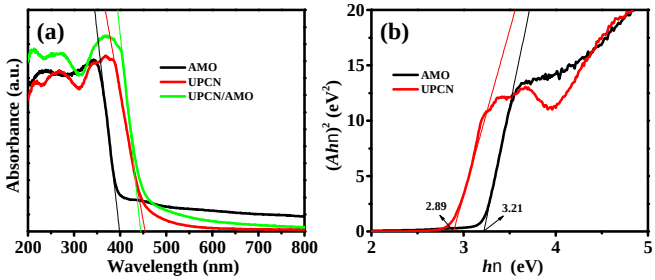

Figure 4. (a) UV-Vis DRS and (b) Tauc curves of various samples.

of C1s orbital at 285.0, 286.3, and 288.3 eV can be indexed to C-C, C-NHx, and N=C-N groups (Figure 3b).[60] While the three characteristic peaks of N1s orbital at 398.5, 399.5, and 400.7 eV can be assigned to C=N-C, N-C3, and C-NH groups (Figure 3c).[28] These typical chemical ingredients are derived from the unique tri-s-triazine structures. Two absorption peaks of Ag 3d orbitals at 367.9 and 373.9 eV come from the Ag^+ ions, while two other absorption peaks at 368.7 and 374.8 eV result from the Ag^0 NPs, indicating a few Ag^+ ions can generate during the process of CO_2 photoreduction (Figure 3d).[39] Two absorption peaks of Mo 3d orbitals at 232.3 and 235.4 eV originate from Mo 3d5/2 and 3d3/2 orbitals (Figure 3e), respectively. Moreover, three adsorption peaks of O 1s orbital at 530.3, 531.8, and 534.5 eV can be indexed to Mo-O, O-H, and Ag-O groups (Figure 3f).[51] Further, the C 1s and N 1s orbitals of UPCN/AMO shift to higher binding energy than that of pristine UPCN, while the Ag 3d, Mo 3d, and O 1s orbitals of UPCN/AMO shift to lower binding energy compared with that of AMO. The results demonstrate that when AMO contacts UPCN, the UPCN loses electrons, while AMO obtains electrons from UPCN.[61]

The light absorption ability and bandgap of samples were uncovered by UV-Vis DRS (Figure 4a). The absorption edge of AMO, UPCN, and UPCN/AMO is 392, 453, and 443 nm, respectively, illustrating that UPCN is the main component of UPCN/AMO and AMO exerts a trivial effect on the visible light-harvesting of UPCN. Further, the bandgap of AMO and UPCN calculated by Tauc relation (Eq. 1) is 3.21 and 2.89 eV, respectively (Figure 4b).[62]

$$\alpha h\upsilon = A(h\upsilon - E_g)^{n/2} \quad (1)$$

Here A, $h\upsilon$, α, and E_g are the constant, photon energy, absorption coefficient, and bandgap of photocatalysts. Besides, both UPCN and AMO are direct semiconductors (n = 1).

$$E_{VB} = X - E^e + 0.5E_g \quad (2)$$

$$E_{CB} = E_{VB} - E_g \quad (3)$$

The electronegativities X of UPCN and AMO are 4.64 and 5.92 eV. The value of constant E^e is 4.5 eV. According to Eq. 1-3, E_{CB} and E_{VB} of UPCN are -1.30 and 1.59 Ev, and those of AMO are -0.18 and 3.03 eV.

The charge generation, migration, recombination, and lifetime were detected by transient photocurrent, Nyquist plots, and SSPL and TRPL spectra (Figure 5). The photocurrent derives from photogenerated charge migration. Compared with pristine AMO and UPCN, the UPCN/AMO composite shows higher transient photocurrent density, revealing that more photogenerated charges are generated under illumination (Figure 5a).[63] The inset in Figure 5b is the equivalent circuit drawing of Nyquist plots. R_s represents

© 2022 fjirsm, CAS, Fuzhou

DOI: 10.14102/j.cnki.0254-5861.2022-0108

Table 1. The TRPL Decay Plots Can Be Fitted by the Multi-exponential Eq. 4.

$I(t) = I_0 + A_1\exp(-t/\tau_1) + A_2\exp(-t/\tau_2) + A_3\exp(-t/\tau_3)$ (4)

$\tau = (A_1\tau_1^2 + A_2\tau_2^2 + A_3\tau_3^2)/(A_1\tau_1 + A_2\tau_2 + A_3\tau_3)$ (5)

where I_0 represent the baseline value; A_i and τ_i (i = 1, 2, 3) are the relative intensity and lifetime indexed to the interior, surficial, and interfacial charge recombination. The average lifetime (τ) is calculated by Eq. 5. The fitting detail is summarized below.

Samples	Decay time (ns)			Relative intensity			Average lifetime (ns)
	τ_1	τ_2	τ_3	A_1	A_2	A_3	
AMO	0.83	6.21	-	4983	327	-	2.60
UPCN	3.17	20.41	-	6881	487	-	8.57
UPCN/AMO	3.02	14.99	0.61	3028	370	7687	5.86

the electrical resistance of the Na_2SO_4 solution. *CPE*$_1$ and *CPE*$_2$ denote the constant phase element between the electrolyte solution and electrode. R_1 signifies the resistance between the conductive glass and photocatalysts. R_{ct} means the charge transfer resistance of samples, expressed by the arc radius of Nyquist plots in the low-frequency region.[64] The UPCN/AMO composite exhibits a smaller arc radius than pristine AMO and UPCN, reflecting a lower charge resistance under light irradiation (Figure 5b). The energy of photocatalysts after charge recombination will be released by fluorescence. Therefore, the SSPL intensity can reveal the recombination degree of the photoexcited charge.[65,66] The UPCN exhibits a vigorous SSPL peak at 475 nm, indicating the intense charge recombination (Figure 5c). Instead, the SSPL intensity of AMO is weak between 400 and 600 nm. The UPCN/AMO composite presents the lowest SSPL intensity, illustrating the charge recombination is well restrained by constructing the UPCN/AMO heterojunction. Further, the TRPL decay curves are employed to explore the photoexcited charge lifetime (Figure 5d). The fitting detail for AMO, UPCN, and UPCN/AMO composite is summarized in Table 1. For pristine AMO, the relative intensity A_1 (4983) of shorter lifetime τ_1 (0.83 ns) far outweighs the relative intensity A_2 (327) of longer lifetime τ_2 (6.21 ns). The same is true for pristine UPCN, illustrating interior photoexcited charge recombination outweighs photocatalyst surface.[62] In contrast, the relative intensity A_1 of UPCN/AMO composite is lower than that of pristine AMO and UPCN, indicating that the interior charge recombination is significantly mitigated. A new lifetime τ_3 (0.61 ns) for UPCN/AMO composite with higher relative intensity A_3 (7687) derives from the interfacial photogenerated charge transfer, thus demonstrating that the interfacial charge transfer contributes to lower interior charge recombination. Therefore, the introduction of AMO boosts the charge separation of UPCN, accounting for a lower average lifetime of UPCN/AMO composite (5.86 ns) than that of pristine UPCN (8.57 ns).

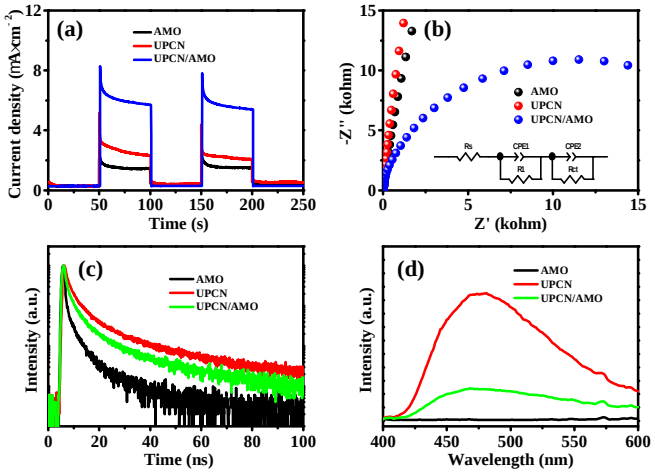

Figure 5. (a) Transient photocurrent, (b) Nyquist plots, (c) SSPL spectra, (d) TRPL decay curves of AMO, UPCN, and UPCN/AMO.

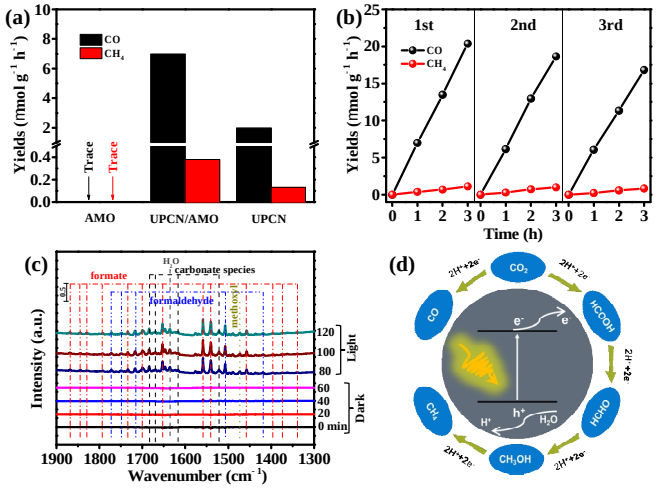

Figure 6. (a) CO_2 photoreduction performance of various samples; (b) Three successive CO_2 photoreduction tests and (c) In situ DRIFTS of UPCN/AMO composite; (d) Illustration of CO_2 photoreduction process.

The photocatalytic activity of UPCN and UPCN/AMO composite was evaluated by CO_2 photoreduction tests conducted under the full spectrum. Due to a weak reduction capability, the pristine AMO has no CO_2 photoreduction activity (Figure 6a).[51] As a comparison, pristine UPCN exhibits high CO_2 photoreduction performance, of which the yield rates of CO and CH_4 are 1.98 and 0.13 μmol g^{-1} h^{-1}. The preferential CO_2 photoconversion to CO for UPCN is consistent with previous reports. The UPCN/AMO composite exhibits high CO_2 photoreduction performance with CO and CH_4 yield rates of 6.98 and 0.38 μmol g^{-1} h^{-1}, which are 3.5 and 2.9 folds higher than that of pristine UPCN, respectively. According to Figure 5, the enhanced CO_2 photoreduction performance is derived from effective charge separation. The photostability of the UPCN/AMO composite was investigated by three successive CO_2 photoreduction tests (Figure 6b). After three runs, the CO and CH_4 yield rates can remain at 83% and 74%, demonstrating satisfied CO_2 photoreduction durability. Meanwhile, the comparison to similar work has been summarized (Table S2). The CO_2 photoreduction intermediates were monitored by in situ DRIFTS (Figure 6c). No available signals can be detected without CO_2 flow and irradiation. Subsequently, when the CO_2 gas with water vapor flows through the sample chamber for 60 min, no apparent adsorption peaks can be observed. Under illumination with CO_2 and water vapor flows, the carbonate species (1552, 1619, 1671, and 1683 cm^{-1}) and H_2O (1636 cm^{-1}) adsorbed on

© 2022 fjirsm, CAS, Fuzhou

DOI: 10.14102/j.cnki.0254-5861.2022-0108

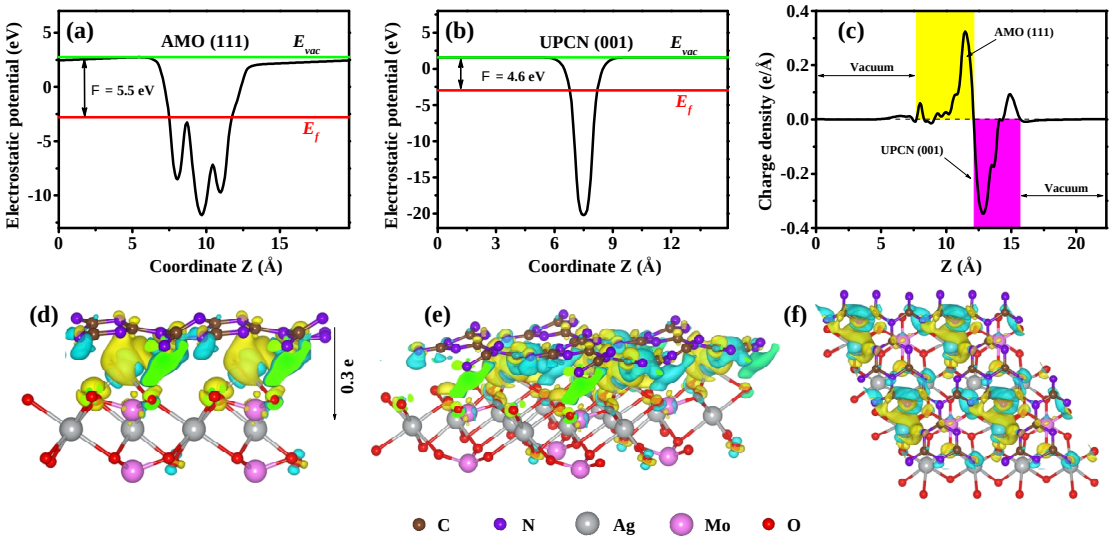

Figure 7. Work function of (a) AMO (111) and (b) UPCN (001) surface; (c) Planar-averaged electron density difference (EDD) $\Delta\rho(z)$ of UPCN (001)/AMO (111) interface; (d,e) Side view and (f) top view of EDD of UPCN (001)/AMO (111) interface with an isosurface of 1.15 × 10^{-3} e/Å^3.

the UPCN/AMO composite surface can be observed.[67] The result uncovers that light excitation can alter the electron density of the UPCN/AMO surface and boost CO_2 and H_2O molecule adsorption. The adsorbed carbonate species and H_2O molecule are the vital precursors of CO_2 photoreduction. Meanwhile, the CO_2 photoreduction products, such as formaldehyde (1419, 1507, 1717, 1749 and 1773 cm^{-1}), formate (1340, 1375, 1396, 1459, 1542, 1559, 1652, 1701, 1734, 1794, 1830, 1846 and 1868 cm^{-1}) and methoxyl (1471 cm^{-1}), can also be clearly observed. The carbonate species and CO_2 photoreduction products change slightly after illumination for 20 min, indicating fast CO_2 adsorption and photoreduction process.[4,68] In addition, the results also discover that the CO and CH_4 derive from the CO_2 photoreduction instead of possible impurities. The CO_2 photoconversion to CH_4 and CO is involved in the synergy of two electrons and two protons (Figure 6d). The reduction of CO_2 to CO takes only one step, while the reduction of CO_2 to CH_4 takes four steps. The adsorbed CO_2 molecule is first catalyzed to HCOOH, then to HCHO, subsequently to CH_3OH, and eventually to CH_4. The complex reduction process can also be a significant factor that the CO yield rate is far higher than the CH_4 one.[67]

To classify the charge separation and transfer mechanism of UPCN/AMO heterojunction, the work function of AMO (111) and UPCN (001) surface and EDD of UPCN (001)/AMO (111) interface were calculated (Figure 7). The work function of AMO (111) and UPCN (001) surface is respectively 5.5 and 4.6 eV (Figure 7a,b). When the vacuum level (E_{Vac}) is defined as zero, the bigger the work function, the more negative the Fermi level (E_f). Therefore, the UPCN E_f is more negative than AMO, indicating when AMO contacts with UPCN, the electron will transfer from UPCN to AMO. The planar-averaged EDD $\Delta\rho(z)$ of UPCN (001)/AMO (111) interface exhibits the electron density of AMO (111) surface is positive (Figure 7c). In contrast, UPCN (001) surface is opposing, which further confirms that electron transfers from UPCN (001) to the AMO (111) surface. To visualize this, the side view (Figure 7d,e) and top view (Figure 7f) of EDD of the UPCN (001)/AMO (111) interface were displayed. The AMO (111) surface is full of yellow, indicating electron accumulation. In contrast, UPCN (001) surface is filled with cyan, denoting the electron depletion, consistent with the work function analysis and planar-averaged EDD $\Delta\rho(z)$. Furthermore, the electron transfer from UPCN (001) to AMO (111) surface quantified by Bader charge is 0.3 e (Figure 7d).

The CO_2 photoreduction mechanism of the S-scheme UPCN/AMO composite was sketchily outlined in Figure 8. First, both UPCN and AMO are n-type semiconductors, and the UPCN CB and E_f are more negative than AMO (Figure 4,7,8a).[41] Therefore, after AMO contacts with UPCN, the UPCN surface will be positively charged due to electron loss, while the AMO surface will be negatively charged owing to electron accumulation (Figure 8b). An IEF directed from UPCN to AMO surface will form. When UPCN/AMO heterojunction is exposed under illumination, the hole will be excited from VB to CB for AMO and UPCN (Figure 8c). The IEF will drive the photoexcited electrons of AMO CB to recombine with the photoexcited holes on UPCN CB. Accordingly, elevated oxidative holes on AMO VB and intensified reductive electrons on UPCN CB will be reserved. Therefore, S-scheme UPCN/

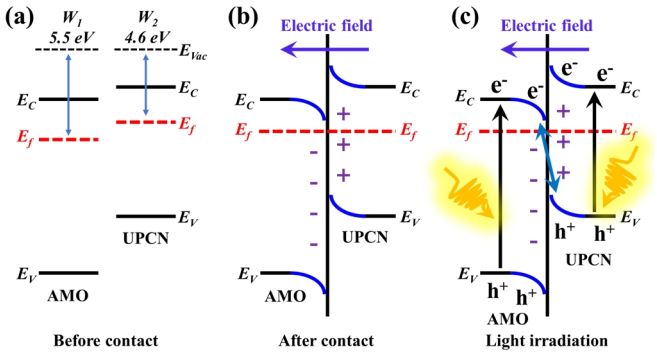

Figure 8. The band structure of UPCN and AMO (a) before and (b) after contact; (c) Charge transfer of UPCN/AMO heterojunction under illumination.

© 2022 fjirsm, CAS, Fuzhou

DOI: 10.14102/j.cnki.0254-5861.2022-0108

AMO heterojunction achieves charge separation, heightens redox capability, and elevates CO_2 photoreduction performance.

n CONCLUSIONS

In summary, S-scheme UPCN/AMO composite is dedicatedly fabricated, responsible for raised CO_2 photoreduction performance. First, the UPCN NSs benefit the load of AMO NPs, which serves as a key for the formation of UPCN/AMO composite. In addition, AMO NPs promote the charge separation of UPCN and reserve the strong redox capability of UPCN/AMO composite by forming S-scheme heterojunction with UPCN. Moreover, the UPCN NSs also provide massive adsorption sites for CO_2 photoreduction. Therefore, the elevated CO_2 photoreduction performance originnates from the ultrathin porous sheet-like structure and S-scheme heterojunction. The design strategy for S-scheme UPCN/AMO can be a reference for the artificial photosynthesis of other UPCN-based composites.

n EXPERIMENTAL

Preparation of UPCN NSs. 12 g urea was transferred a 50 mL crucible and maintained at 550 °C for 2 h in the air. After cooling, the multilayered CN remained. Then the natural CN multilayer was heated to 600 °C for 2 h in the air to generate UPCN NSs.[69]

Preparation of UPCN/AMO Composite and Butterfly-like AMO NSs. Typically, CH_3COOAg (167 mg) and polyvinyl pyrrolidone (833 mg) were successively put in 50 mL deionized water. Then 375 mg UPCN NSs was added and stirred for a while to ensure these UPCN NSs were sufficiently dispersed. Then, $(NH_4)_6Mo_7O_{24}\cdot 4H_2O$ (28.5 mM, 2.5 mL) was poured carefully to load the AMO on UPCN NSs. Ultimately, the UPCN/AMO was collected by washing and drying. The butterfly-like AMO NSs were synthesized in the same route without introducing the UPCN NSs.

Characterization. Morphology with elemental distribution was observed on JSM 7500F field emission scanning electron microscope (FESEM), Titan G2 60-300 transmission electron microscopy (TEM), Bruker MultiMode 8 atomic force microscope (AFM), and aberration-corrected high-angle annular dark-field scanning transmission electron microscopy (HAADF-STEM) with energy dispersive X-ray spectrometer (EDS). X-ray diffraction (XRD) patterns and N_2 adsorption-desorption (CO_2 adsorption) spectra were recorded on Shimadzu XRD-6100 X-ray diffractometer and a Micromeritics ASAP 3020 nitrogen adsorption instrument. XPS was recorded on the Thermo ESCALAB 250Xi apparatus. Electron paramagnetic resonance (EPR) spectroscopy and UV-Vis diffuse reflectance spectra (DRS) were respectively collected on Bruker EXM nano EPR spectrometer and Shimadzu UV-2600 UV-Vis spectrophotometer. Fourier transform infrared (FT-IR) and in-situ DRIFTS were obtained from the Nicolet iS50 spectrometer. Photoelectrochemical tests and SSPL (TRPL) spectra were collected on the CHI660C electrochemical workstation and FLS1000 fluorescence spectrophotometer, respectively.

CO_2 Photoreduction Test and Computational Details. It is provided in supporting information.

n ACKNOWLEDGEMENTS

This work was supported by the National Natural Science Foundation of China (51572103 and 51973078), the Distinguished Young Scholar of Anhui Province (1808085J14), the Major Projects of Education Department of Anhui Province (KJ2020ZD005), and the Key Foundation of Educational Commission of Anhui Province (KJ2019A0595).

n AUTHOR INFORMATION

Corresponding authors. Fax: +86-561-3803256. Emails: daikai940@chnu.edu.cn (K. Dai) and jfzhang@chnu.edu.cn (J. Zhang)

n COMPETING INTERESTS

The authors declare no competing interests.

n ADDITIONAL INFORMATION

Supplementary information is available for this paper at http://manu30.magtech.com.cn/jghx/EN/10.14102/j.cnki.0254-5861.2022-0108

For submission: https://mc03.manuscriptcentral.com/cjsc

n REFERENCES

(1) Zhang, L.; Zhang, J.; Yu, H.; Yu, J. Emerging S-Scheme photocatalyst. *Adv. Mater.* **2022**, 34, 2107668.

(2) Li, Y.; Zhang, M.; Zhou, L.; Yang, S.; Wu, Z.; Ma, Y. Recent advances in surface-modified g-C_3N_4-based photocatalysts for H_2 production and CO_2 reduction. *Acta Phys. Chim. Sin.* **2021**, 37, 2009030.

(3) Wageh, S.; Al-Hartomy, O. A.; Alotaibi, M. F.; Liu, L. Ionized cocatalyst to promote CO_2 photoreduction activity over core-triple-shell ZnO hollow spheres. *Rare Metals* **2022**, 41, 1077-1079.

(4) Wang, L.; Cheng, B.; Zhang, L.; Yu, J. In situ irradiated XPS investigation on S-scheme TiO_2@$ZnIn_2S_4$ photocatalyst for efficient photocatalytic CO_2 reduction. *Small* **2021**, 17, 2103447.

(5) Ke, X.; Zhang, J.; Dai, K.; Fan, K.; Liang, C. Integrated S-scheme heterojunction of amine-functionalized 1D CdSe nanorods anchoring on ultrathin 2D $SnNb_2O_6$ nanosheets for robust solar-driven CO_2 conversion. *Solar RRL* **2021**, 5, 2000805.

(6) Liu, S.; Chen, W.; Li, Y.; Ding, K.; Zhang, Y.; Lin, W. Mechanism on carbon vacancies in polymeric carbon nitride for CO_2 rhotoreduction. *Chin. J. Struct. Chem.* **2020**, 39, 2068-2076.

(7) Mei, Z.; Wang, G.; Yan, S.; Wang, J. Rapid microwave-assisted synthesis of 2D/1D $ZnIn_2S_4$/TiO_2 S-scheme heterojunction for catalyzing photocatalytic hydrogen evolution. *Acta Phys. Chim. Sin.* **2021**, 37, 2009097.

(8) Zhang, J.; Fu, J.; Dai, K. Graphitic carbon nitride/antimonene van der Waals heterostructure with enhanced photocatalytic CO_2 reduction activity. *J. Mater. Sci. Technol.* **2022**, 116, 192-198.

(9) Zhang, H.-X.; Hong, Q.-L.; Li, J.; Wang, F.; Huang, X.; Chen, S.; Tu, W.; Yu, D.; Xu, R.; Zhou, T.; Zhang, J. Isolated square-planar copper center in boron imidazolate nanocages for photocatalytic reduction of CO_2 to CO. *Angew. Chem. Int. Ed.* **2019**, 58, 11752-11756.

(10) Sayed, M.; Xu, F.; Kuang, P.; Low, J.; Wang, S.; Zhang, L.; Yu, J. Sustained CO_2-photoreduction activity and high selectivity over Mn, C-codoped ZnO core-triple shell hollow spheres. *Nat. Commun.* **2021**, 12, 4936.

(11) Wang, Z.; Fan, J.; Cheng, B.; Yu, J.; Xu, J. Nickel-based cocatalysts for photocatalysis: hydrogen evolution, overall water splitting and CO_2 reduction. *Mater. Today Phys.* **2020**, 15, 100279.

© 2022 fjirsm, CAS, Fuzhou

DOI: 10.14102/j.cnki.0254-5861.2022-0108

(12) Shao, P.; Yi, L.; Chen, S.; Zhou, T.; Zhang, J. Metal-organic frameworks for electrochemical reduction of carbon dioxide: the role of metal centers. *J. Energy Chem.* **2020**, 40, 156-170.
(13) Liu, M.-R.; Hong, Q.-L.; Li, Q.-H.; Du, Y.; Zhang, H.-X.; Chen, S.; Zhou, T.; Zhang, J. Cobalt boron imidazolate framework derived cobalt nanoparticles encapsulated in B/N codoped nanocarbon as efficient bifunctional electrocatalysts for overall water splitting. *Adv. Funct. Mater.* **2018**, 28, 1801136.
(14) Fei, X.; Tan, H.; Cheng, B.; Zhu, B.; Zhang, L. 2D/2D black phosphorus/g-C_3N_4 S-scheme heterojunction photocatalysts for CO_2 reduction investigated using DFT calculations. *Acta Phys. Chim. Sin.* **2021**, 37, 2010027.
(15) Mei, F.; Dai, K.; Zhang, J.; Li, L.; Liang, C. Ultrathin indium vanadate/cadmium selenide-amine step-scheme heterojunction with interfacial chemical bonding for promotion of visible-light-driven carbon dioxide reduction. *J. Colloid Interf. Sci.* **2022**, 608, 1846-1856.
(16) Wageh, S.; Al-Ghamdi, A. A.; Liu, L. S-Scheme heterojunction photocatalyst for CO_2 photoreduction. *Acta Phys. Chim. Sin.* **2021**, 37, 2010024.
(17) Sayed, M.; Zhu, B.; Kuang, P.; Liu, X.; Cheng, B.; Al Ghamdi, A.; Wageh, S.; Zhang, L.; Yu, J. EPR investigation on electron transfer of 2D/3D g-C_3N_4/ZnO S-scheme heterojunction for enhanced CO_2 photoreduction. *Adv. Sustain. Syst.* **2022**, 6, 2100264.
(18) Zhou, T.; Du, Y.; Borgna, A.; Hong, J.; Wang, Y.; Han, J.; Zhang, W.; Xu, R. Post-synthesis modification of a metal-organic framework to construct a bifunctional photocatalyst for hydrogen production. *Energy Environ. Sci.* **2013**, 6, 3229-3234.
(19) Li, M.; Guan, R.; Li, J.; Zhao, Z.; Zhang, J.; Dong, C.; Qi, Y.; Zhai, H. Performance and mechanism research of Au-HSTiO_2 on photocatalytic hydrogen production. *Chin. J. Struct. Chem.* **2020**, 39, 1437-1443.
(20) Wang, P.; Li, H.; Cao, Y.; Yu, H. Carboxyl-functionalized graphene for highly efficient H_2-evolution activity of TiO_2 photocatalyst. *Acta Phys. Chim. Sin.* **2021**, 37, 2008047.
(21) Zhang, J.; Liao, H.; Sun, S. Construction of 1D/1D WO_3 nanorod/TiO_2 nanobelt hybrid heterostructure for photocatalytic application. *Chin. J. Struct. Chem.* **2020**, 39, 1019-1028.
(22) Li, J.; Wu, X.; Liu, S. Fluorinated TiO_2 hollow photocatalysts for photocatalytic applications. *Acta Phys. Chim. Sin.* **2021**, 37, 2009038.
(23) Jiang, X.; Chen, Y.; Lu, C. Bio-inspired materials for photocatalytic hydrogen production. *Chin. J. Struct. Chem.* **2020**, 39, 2123-2130.
(24) Li, S.; Cai, M.; Liu, Y.; Zhang, J.; Wang, C.; Zang, S.; Li, Y.; Zhang, P.; Li, X. In situ construction of a C_3N_5 nanosheet/Bi_2WO_6 nanodot S-scheme heterojunction with enhanced structural defects for the efficient photocatalytic removal of tetracycline and Cr(VI). *Inorg. Chem. Front.* **2022**, 9, 2479-2497.
(25) Wang, D.; Yin, F.; Cheng, B.; Xia, Y.; Yu, J.; Ho, W. Enhanced photocatalytic activity and mechanism of CeO_2 hollow spheres for tetracycline degradation. *Rare Metals* **2021**, 40, 2369-2380.
(26) Zhu, B.; Cheng, B.; Fan, J.; Ho, W.; Yu, J. g-C_3N_4-Based 2D/2D composite heterojunction photocatalyst. *Small Struct.* **2021**, 2, 2100086.
(27) Li, X.; Liu, J.; Huang, J.; He, C.; Feng, Z.; Chen, Z.; Wan, L.; Deng, F. All organic S-scheme heterojunction PDI-Ala/S-C_3N_4 photocatalyst with enhanced photocatalytic performance. *Acta Phys. Chim. Sin.* **2021**, 37, 2010030.
(28) Li, X.; Zhang, J.; Huo, Y.; Dai, K.; Li, S.; Chen, S. Two-dimensional sulfur- and chlorine-codoped g-C_3N_4/CdSe-amine heterostructures nanocomposite with effective interfacial charge transfer and mechanism insight. *Appl. Catal. B: Environ.* **2021**, 280, 119452.
(29) Bie, C.; Cheng, B.; Fan, J.; Ho, W.; Yu, J. Enhanced solar-to-chemical energy conversion of graphitic carbon nitride by two-dimensional co-catalysts. *EnergyChem* **2021**, 3, 100051.
(30) Chen, Y.; Li, L.; Xu, Q.; Düren, T.; Fan, J.; Ma, D. Controllable synthesis of g-C_3N_4 inverse opal photocatalysts for superior hydrogen evolution. *Acta Phys. Chim. Sin.* **2021**, 37, 2009080.
(31) Shen, R.; Lu, X.; Zheng, Q.; Chen, Q.; Ng, Y. H.; Zhang, P.; Li, X. Tracking S-scheme charge transfer pathways in Mo_2C/CdS H_2-evolution photocatalysts. *Solar RRL* **2021**, 5, 2100177.
(32) Zhao, Z.; Li, X.; Dai, K.; Zhang, J.; Dawson, G. In-situ fabrication of Bi_2S_3/$BiVO_4$/$Mn_{0.5}Cd_{0.5}S$-DETA ternary S-scheme heterostructure with effective interface charge separation and CO_2 reduction performance. *J. Mater. Sci. Technol.* **2022**, 117, 109-119.
(33) He, F.; Zhu, B.; Cheng, B.; Yu, J.; Ho, W.; Macyk, W. 2D/2D/0D TiO_2/C_3N_4/Ti_3C_2 MXene composite S-scheme photocatalyst with enhanced CO_2 reduction activity. *Appl. Catal. B: Environ.* **2020**, 272, 119006.
(34) Guo, H.; Ding, J.; Wan, S.; Wang, Y.; Zhong, Q. Highly efficient CH_3OH production over $Zn_{0.2}Cd_{0.8}S$ decorated g-C_3N_4 heterostructures for the photoreduction of CO_2. *Appl. Surf. Sci.* **2020**, 528, 146943.
(35) Huo, Y.; Zhang, J.; Dai, K.; Li, Q.; Lv, J.; Zhu, G.; Liang, C. All-solid-state artificial Z-scheme porous g-C_3N_4/Sn_2S_3-DETA heterostructure photocatalyst with enhanced performance in photocatalytic CO_2 reduction. *Appl. Catal. B: Environ.* **2019**, 241, 528-538.
(36) Thanh Truc, N. T.; Hanh, N. T.; Nguyen, M. V.; Le Chi, N. T. P.; Van Noi, N.; Tran, D. T.; Ha, M. N.; Trung, D. Q.; Pham, T.-D. Novel direct Z-scheme $Cu_2V_2O_7$/g-C_3N_4 for visible light photocatalytic conversion of CO_2 into valuable fuels. *Appl. Surf. Sci.* **2018**, 457, 968-974.
(37) Liang, M.; Borjigin, T.; Zhang, Y.; Liu, H.; Liu, B.; Guo, H. Z-Scheme Au@Void@g-C_3N_4/SnS yolk-shell heterostructures for superior photocatalytic CO_2 reduction under visible light. *ACS Appl. Mater. Interfaces* **2018**, 10, 34123-34131.
(38) Li, M.; Zhang, L.; Fan, X.; Wu, M.; Wang, M.; Cheng, R.; Zhang, L.; Yao, H.; Shi, J. Core-shell $LaPO_4$/g-C_3N_4 nanowires for highly active and selective CO_2 reduction. *Appl. Catal. B: Environ.* **2017**, 201, 629-635.
(39) Wang, Z.; Zhang, J.; Lv, J.; Dai, K.; Liang, C. Plasmonic Ag_2MoO_4/AgBr/Ag composite: excellent photocatalytic performance and possible photocatalytic mechanism. *Appl. Surf. Sci.* **2017**, 396, 791-798.
(40) Tang, H.; Lu, A.; Li, L.; Zhou, W.; Xie, Z.; Zhang, L. Highly antibacterial materials constructed from silver molybdate nanoparticles immobilized in chitin matrix. *Chem. Eng. J.* **2013**, 234, 124-131.
(41) Huo, Y.; Wang, Z.; Zhang, J.; Liang, C.; Dai, K. Ag SPR-promoted 2D porous g-C_3N_4/Ag_2MoO_4 composites for enhanced photocatalytic performance towards methylene blue degradation. *Appl. Surf. Sci.* **2018**, 459, 271-280.
(42) Yu, W.; Xu, D.; Peng, T. Enhanced photocatalytic activity of g-C_3N_4 for selective CO_2 reduction to CH_3OH via facile coupling of ZnO: a direct Z-scheme mechanism. *J. Mater. Chem. A* **2015**, 3, 19936-19947.
(43) Lin, H.; Xu, Y.; Wang, B.; Li, D.-S.; Zhou, T.; Zhang, J. Postsynthetic modification of metal-organic frameworks for photocatalytic applications. *Small Struct.* **2022**, 3, 2270018.
(44) Zhou, T.; Wang, D.; Chun-Kiat Goh, S.; Hong, J.; Han, J.; Mao, J.; Xu, R. Bio-inspired organic cobalt(II) phosphonates toward water oxidation. *Energy Environ. Sci.* **2015**, 8, 526-534.
(45) He, R.; Chen, R.; Luo, J.; Zhang, S.; Xu, D. Fabrication of graphene quantum dots modified BiOI/PAN flexible fiber with enhanced photocata-

 © 2022 fjirsm, CAS, Fuzhou
DOI: 10.14102/j.cnki.0254-5861.2022-0108

lytic activity. *Acta Phys. Chim. Sin.* **2021**, 37, 2011022.
(46) Wang, C.; Li, S.; Cai, M.; Yan, R.; Dong, K.; Zhang, J.; Liu, Y. Rationally designed tetra (4-carboxyphenyl) porphyrin/graphene quantum dots/bismuth molybdate Z-scheme heterojunction for tetracycline degradation and Cr(VI) reduction: Performance, mechanism, intermediate toxicity appraisement. *J. Colloid Interf. Sci.* **2022**, 619, 307-321.
(47) Zhou, T.; Du, Y.; Wang, D.; Yin, S.; Tu, W.; Chen, Z.; Borgna, A.; Xu, R. Phosphonate-based metal-organic framework derived Co-P-C hybrid as an efficient electrocatalyst for oxygen evolution reaction. *ACS Catal.* **2017**, 7, 6000-6007.
(48) Wang, Z.; Dai, K.; Liang, C.; Zhang, J.; Zhu, G. Facile synthesis of novel butterfly-like Ag_2MoO_4 nanosheets for visible-light driven photocatalysis. *Mater. Lett.* **2017**, 196, 373-376.
(49) Lin, H.; Chen, C.; Zhou, T.; Zhang, J. Two-dimensional covalent-organic frameworks for photocatalysis: the critical roles of building block and linkage. *Solar RRL* **2021**, 5, 2000458.
(50) Huang, Y.; Mei, F.; Zhang, J.; Dai, K.; Dawson, G. Construction of 1D/2D $W_{18}O_{49}$/porous g-C_3N_4 S-scheme heterojunction with enhanced photocatalytic H_2 evolution. *Acta Phys. Chim. Sin.* **2022**, 38, 2108028.
(51) Wang, Z.; Huo, Y.; Zhang, J.; Lu, C.; Dai, K.; Liang, C.; Zhu, G. Facile preparation of two-dimensional Bi_2MoO_6@Ag_2MoO_4 core-shell composite with enhanced visible light photocatalytic activity. *J. Alloys Compd.* **2017**, 729, 100-108.
(52) Li, S.; Wang, C.; Cai, M.; Liu, Y.; Dong, K.; Zhang, J. Designing oxygen vacancy mediated bismuth molybdate (Bi_2MoO_6)/N-rich carbon nitride (C_3N_5) S-scheme heterojunctions for boosted photocatalytic removal of tetracycline antibiotic and Cr(VI): Intermediate toxicity and mechanism insight. *J. Colloid Interf. Sci.* **2022**, 624, 219-232.
(53) Li, X.; Zhang, J.; Dai, K.; Fan, K.; Liang, C. $Cd_3(C_3N_3S_3)_2$ polymer/Sn Schottky heterojunction for broadband-solar highly selective photocatalytic CO_2 reduction. *Solar RRL* **2021**, 5, 2100788.
(54) Huo, Y.; Zhang, J.; Wang, Z.; Dai, K.; Pan, C.; Liang, C. Efficient interfacial charge transfer of 2D/2D porous carbon nitride/bismuth oxychloride step-scheme heterojunction for boosted solar-driven CO_2 reduction. *J. Colloid Interf. Sci.* **2021**, 585, 684-693.
(55) Li, Z.; Wu, Z.; He, R.; Wan, L.; Zhang, S. $In_2O_{3-x}(OH)_y$/Bi_2MoO_6 S-scheme heterojunction for enhanced photocatalytic performance. *J. Mater. Sci. Technol.* **2020**, 56, 151-161.
(56) Xia, P.; Cao, S.; Zhu, B.; Liu, M.; Shi, M.; Yu, J.; Zhang, Y. Designing a 0D/2D S-scheme heterojunction over polymeric carbon nitride for visible-light photocatalytic inactivation of bacteria. *Angew. Chem. Int. Ed.* **2020**, 59, 5218-5225.
(57) Bai, J.; Shen, R.; Jiang, Z.; Zhang, P.; Li, Y.; Li, X. Integration of 2D layered CdS/WO_3 S-scheme heterojunctions and metallic Ti_3C_2 MXene-based Ohmic junctions for effective photocatalytic H_2 generation. *Chin. J. Catal.* **2022**, 43, 359-369.
(58) Liu, T.; Zhou, S.; Qi, J.; Wang, K.; Zheng, L.; Huang, Q.; Zhou, T.; Zhang, J. Engineering nanointerface of molybdenum-based heterostructures to boost the electrocatalytic hydrogen evolution reaction. *J. Energy Chem.* **2021**, 58, 370-376.
(59) Li, S.; Cai, M.; Wang, C.; Liu, Y.; Li, N.; Zhang, P.; Li, X. Rationally designed Ta_3N_5/BiOCl S-scheme heterojunction with oxygen vacancies for elimination of tetracycline antibiotic and Cr(VI): performance, toxicity evaluation and mechanism insight. *J. Mater. Sci. Technol.* **2022**, 123, 177-190.
(60) Wang, Z.; Lv, J.; Zhang, J.; Dai, K.; Liang, C. Facile synthesis of Z-scheme $BiVO_4$/porous graphite carbon nitride heterojunction for enhanced visible-light-driven photocatalyst. *Appl. Surf. Sci.* **2018**, 430, 595-602.
(61) Xu, F.; Meng, K.; Cao, S.; Jiang, C.; Chen, T.; Xu, J.; Yu, J. Step-by-step mechanism insights into the TiO_2/Ce_2S_3 S-scheme photocatalyst for enhanced aniline production with water as a proton source. *ACS Catal.* **2021**, 12, 164-172.
(62) Wang, Z.; Cheng, B.; Zhang, L.; Yu, J.; Li, Y.; Wageh, S.; Al-Ghamdi, A. A. S-Scheme 2D/2D Bi_2MoO_6/BiOI van der Waals heterojunction for CO_2 photoreduction. *Chin. J. Catal.* **2022**, 43, 1657-1666.
(63) Yang, H.; Zhang, J. F.; Dai, K. Organic amine surface modified one-dimensional $CdSe_{0.8}S_{0.2}$-diethylenetriamine/two-dimensional $SnNb_2O_6$ S-scheme heterojunction with promoted visible-light-driven photocatalytic CO_2 reduction. *Chin. J. Catal.* **2022**, 43, 255-264.
(64) Hu, T.; Dai, K.; Zhang, J.; Chen, S. Noble-metal-free Ni_2P modified step-scheme $SnNb_2O_6$/CdS-diethylenetriamine for photocatalytic hydrogen production under broadband light irradiation. *Appl. Catal. B: Environ.* **2020**, 269, 118844.
(65) Li, S.; Wang, C.; Cai, M.; Yang, F.; Liu, Y.; Chen, J.; Zhang, P.; Li, X.; Chen, X. Facile fabrication of TaON/Bi_2MoO_6 core-shell S-scheme heterojunction nanofibers for boosting visible-light catalytic levofloxacin degradation and Cr(VI) reduction. *Chem. Eng. J.* **2022**, 428, 131158.
(66) Shen, R.; Hao, L.; Ng, Y. H.; Zhang, P.; Arramel, A.; Li, Y.; Li, X. Heterogeneous N-coordinated single-atom photocatalysts and electrocatalysts. *Chin. J. Catal.* **2022**, DOI: 10.1016/s1872-2067(1022)64104-64104.
(67) Wang, Z.; Cheng, B.; Zhang, L.; Yu, J.; Tan, H. BiOBr/NiO S-scheme heterojunction photocatalyst for CO_2 photoreduction. *Solar RRL* **2022**, 6, 2100587.
(68) Deng, H.; Fei, X.; Yang, Y.; Fan, J.; Yu, J.; Cheng, B.; Zhang, L. S-scheme heterojunction based on p-type $ZnMn_2O_4$ and n-type ZnO with improved photocatalytic CO_2 reduction activity. *Chem. Eng. J.* **2021**, 409, 127377.
(69) Lei, G.; Cao, Y.; Zhao, W.; Dai, Z.; Shen, L.; Xiao, Y.; Jiang, L. Exfoliation of graphitic carbon nitride for enhanced oxidative desulfurization: a facile and general strategy. *ACS Sustain. Chem. Eng.* **2019**, 7, 4941-4950.

Received: May 4, 2022
Accepted: May 29, 2022
Published: June 20, 2022

© 2022 fjirsm, CAS, Fuzhou

DOI: 10.14102/j.cnki.0254-5861.2022-0108